Lithuanian Journal of Physics
Vol. **65**, No. 1, pp. 57–71 (2025)
ISSN 1648-8504 eISSN 2424-3647
DOI: https://doi.org/10.3952/physics.2025.65.1.5

HIGH-FREQUENCY CONDUCTIVITY-BASED TERAHERTZ GAIN MODELS IN QUANTUM SEMICONDUCTOR SUPERLATTICES: A COMPARATIVE STUDY

L. Stakėla, K.N. Alekseev, and G. Valušis

Department of Optoelectronics, Center for Physical Sciences and Technology, Saulėtekio 3, 10257 Vilnius, Lithuania
Email: lukas.stakela@ftmc.lt

Received 19 December 2024; accepted 17 January 2025

The development of high-power, stable and portable terahertz (THz) sources that can operate at room temperature remains one of the biggest challenges in THz and solid-state physics. Despite modern semiconductor devices such as resonant tunnelling diodes and quantum cascade lasers demonstrating a significant progress, they still face several limitations related to a low power output, temperature sensitivity and the lack of frequency tunability. In this respect, semiconductor superlattices operating in the miniband transport regime continue to represent promising quantum materials for the realization of the desirable THz gain. In this study, we briefly overview basic semiclassical models describing the high-frequency conductivity of superlattices. We cover the popular model of Ktitorov et al. and the lesser-known and more advanced model of Ignatov and Shashkin, and also make their comparative analysis with reference to the classical quasistatic model of gain in devices with the negative differential conductivity. This work aims to offer a simple introduction to these models and their practical relevance to THz device design and development.

Keywords: semiconductor superlattices, negative differential conductivity, terahertz gain

1. Introduction

The terahertz (THz) frequency range (1 THz is 10^{12} Hz) nestled between the microwaves and infrared ranges in the electromagnetic spectrum displays an exciting ability to propagate with minimal losses in numerous dielectric materials and compounds. This remarkable feature exhibited THz imaging and spectroscopy as powerful instruments in a contactless inspection of various materials, for security checks and industrial applications [1]. THz radiation attracts a surging interest in THz wireless communications [2], due to possibilities in applications of high-definition video streaming, virtual reality and augmented reality as well as the ability to transmit data in terabits per second range [3].

However, one of the biggest challenges in the progress of direct implementation of THz frequencies remains the development of high-power, stable and portable THz sources operating at room temperature. Particular attention is attributed to solid-state and semiconductor-based devices as they enable compact dimensions of the systems, convenience in use and the effective power consumption [1]. Semiconductor nanostructure-based devices such as resonant tunnelling diodes [4] and quantum cascade lasers [5] show a promising potential; however, they still face limitations related to a relatively low power output, temperature-sensitive operational conditions and the lack of frequency tunability.

A rational route to overcome these hurdles could be related to the employment of semiconductor superlattices (SSLs) [6, 7]. Superlattices are heterostructures made of alternating semiconductor materials, commonly GaAs/$Al_xGa_{1-x}As$, to create energy minibands via the control of quantum

well and barrier thicknesses (see Fig. 2). SSLs are typically fabricated either by molecular beam epitaxy or by doping a single material to create structures of alternating *n*-, *i*- and *p*-type regions which are commonly known as *n*-*i*-*p*-*i* type superlattices. As in periodic crystal lattices, these alternating quantum wells create a periodic profile of the potential energy resulting in the formation of several energy minibands. Variation of the materials content and thickness of wells/barriers enables tailoring the widths of minibands and gaps, and hence controlling the carrier transport in a desirable way. In particular, the electron transport under the action of modest electric fields can be limited to a single miniband – this is known as the miniband transport regime and it is of the primary interest in the present paper. Perhaps, one of the most peculiar field-induced effects observable in the miniband is ultrafast Bloch oscillations [8–10] – periodic oscillations of optically excited electron wave packets both in time and in space. The phenomenon occurs at the THz range and is coherent, i.e. to make the observation of Bloch oscillations possible, scattering processes should be eliminated from the direct influence on the coherent wave-packet motion. The frequency of Bloch oscillations is tuneable by the applied electric field, thus opening an avenue to design an electric field tuneable THz emitter.

Furthermore, in the stationary electron transport, superlattices exhibit remarkable features of negative differential conductivity (NDC) as was indicated in the pioneering work by Esaki and Tsu [6]. This makes SSL an attractive platform for the realization of electrically driven GHz-THz oscillators [11] and amplifiers [12]. To understand the transition from absorption to gain and to estimate the limiting frequencies of the active devices with NDC, one needs to calculate the high-frequency conductivity of the structure, which describes its linear response to a small periodic signal. At a very high frequency of the signal, the complex conductivity can demonstrate temporal and spatial dispersions. Specifically for SSLs, the effect of high-frequency gain due to NDC is often called Bloch gain [13, 14].

The Bloch gain displays dispersive features which are in a sharp contrast to those of classical oscillators, as illustrated in Fig. 1. For the classical linear oscillator driven by the electric field of high-frequency ω, the real part of complex conductivity is positive exhibiting the absorption

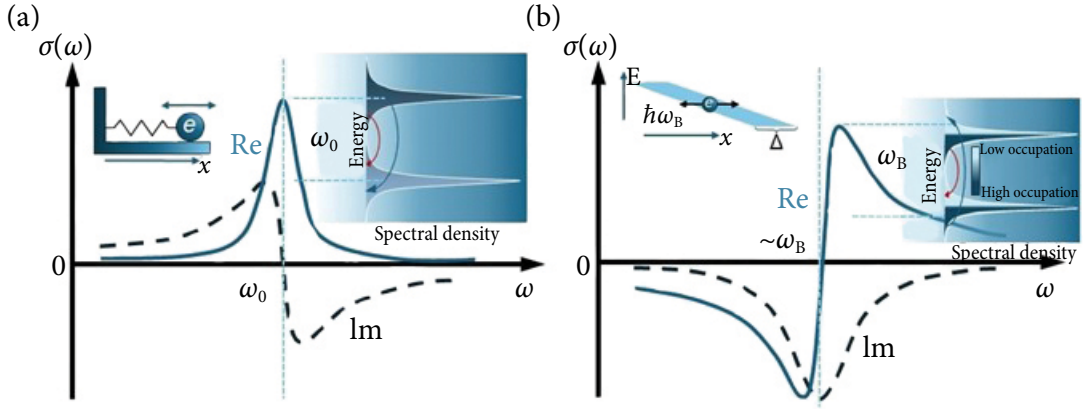

Fig. 1. Illustrative comparison of the properties of a semiclassical charged harmonic oscillator (panel (a)) and a Bloch oscillator (panel (b)) in a frequency domain. The real parts of conductivity are represented by a solid blue line, while the imaginary parts are shown by dashed lines. Note always positive conductivity in the case of harmonic oscillator and the dispersive origin of Bloch gain manifesting itself as negative real part of conductivity below the Bloch frequency ω_B and the absorption above it according to the Ktitorov's model. Left insets in panel (a) and panel (b) represent the harmonic oscillator and the Bloch oscillator in a superlattice with a miniband width Δ, respectively. Right insets show the optical illustration of the gain with a population inversion panel (a) and the inversionless Bloch gain in superlattices presented in panel (b) (adapted from [15]). Note a nonuniform occupancy of carrier distributions in broadened transition lines.

line of Lorentzian shape, while its imaginary part has a familiar dispersive shape. The real part of conductivity is peaked at the natural (or eigen) frequency ω_0 of the oscillator indicating the maximum loss, and there is no pronounced gain. In the case of Bloch oscillator, the picture is essentially different – the real part of conductivity is negative below the frequency of Bloch oscillations ω_B, demonstrating the presence of the broadband Bloch gain. When the incident radiation coincides exactly with the Bloch frequency, the dispersion curve changes its sign representing that the system exhibits neither gain nor absorption at the Bloch resonance, i.e. the structure is transparent. With further increase of frequency, i.e. $\omega > \omega_B$, the conductivity becomes always positive manifesting pronounced absorption. It is worth noting that the Bloch gain displays two distinctive features in comparison to the conventional optical gain in laser physics: the Bloch gain is inversionless and dispersive because of its inhomogeneously broadened linewidth and scattering assistant transitions [15]. One needs to recall that the gain in lasers requires population inversion at the natural frequency of transition.

There are two seminal models describing physics behind the crossover from absorption to gain in SSLs. The first one is the minimal semiclassical high-frequency conductivity model of Ktitorov–Simin–Sindalovskii (KSS) [16], and the other one is the more specialized Ignatov–Shashkin (IS) model which addresses high-frequency properties of space-charge waves [17]. While these models are rooted in similar physical principles and are based on perturbative solutions of the Boltzmann transport equation for a single miniband, they differ in several assumptions and mathematical formulations, leading to distinct predictions for high-frequency electron transport properties. In the present work, we provide a comparative overview and side-by-side analysis of the both models, underlying the importance of temporal and spatial dispersion effects caused by Bloch oscillations. We also briefly discuss the practical relevance of these and other superlattice models to GHz-THz device development.

The paper is organized as follows. Section 2 provides a theoretical background, including an introduction to the high-frequency conductivity and quasistatic model, while Section 3 reviews the Ktitorov's model [16]. Furthermore, Section 4 presents the Ignatov–Shashkin model [17], with careful attention to the underlying assumptions and mathematical framework. Section 5 offers a comparative analysis of Ignatov's and Ktitorov's high-frequency conductivity models using numerical calculations. Finally, Section 6 provides some extensions of the models, the related experimental insights and outlook.

2. Overview of electron transport in semiconductor superlattices

Superlattices exhibit unique optical and electronic high-frequency properties compared to traditional bulk semiconductors mainly due to their significantly longer lattice constant [18].

In particular, this structural feature of SSLs allows for the observation of such remarkable high-frequency phenomena as electron Bloch oscillations under the action of already *moderate* electric field (~10 kV/cm). Indeed, this coherent ultrafast effect is characterized by the Bloch frequency

$$\omega_B = \frac{eE_0 d}{\hbar}, \tag{1}$$

where E_0 is the strength of the constant electric field, d is the superlattice period, e is the elementary charge, ħ is the reduced Planck's constant, and it has been assumed that all oscillating electrons belong to the same first miniband. It is easy to see from Eq. (1) that for the typical spatial period of several nanometres the Bloch frequency $\omega_B/2\pi$ belongs to the THz range, and therefore it is quite possible to excite one or even many Bloch cycles on the timescale shorter than the characteristic scattering time $\tau \sim 0.1$ ps at room temperature. In the energy representation, the Bloch frequency corresponds to transitions between equally spaced ($\hbar\omega_B$) energy levels, known as Wannier–Stark ladder. Therefore, along with ultrafast optical measurements [8, 9], the Bloch oscillations are also observable in the frequency domain via the manifestation of the Wannier–Stark ladder effects in the optical spectra of SSLs [19, 20].

When the static electric field is applied to an SSL structure, electrons traverse the k space towards the Brillouin zone (BZ) boundary at $k' = \pi/d$ (See Fig. 3).

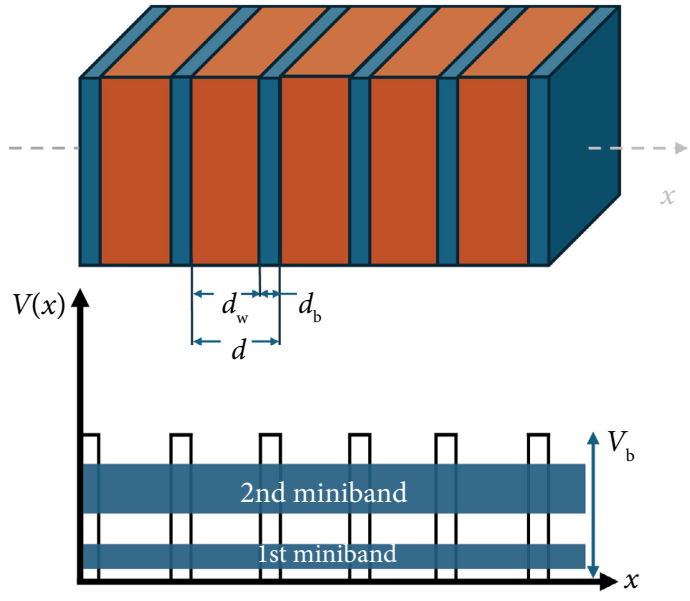

Fig. 2. Schematic representation of a semiconductor superlattice (SSL) (top panel) and its potential profile with minibands (bottom panel). Differently coloured sections represent separate or differently doped materials. d_w and d_b denote the width of the well and the barrier, respectively, the SL period is $d = d_w + d_b$, and V_b is the potential height of the barrier. The x axis depicts the axis of the superlattice. In contrast to the current convention, we denoted the SSL axis as the x axis for the convenience of readers in comparing the given description with the theoretical works by Ktitorov and Ignatov [16, 17].

Within the tight-binding approximation, the electron energy is described as

$$\varepsilon = \frac{\Delta}{2}(1 - \cos(\mathrm{d}k')), \tag{2}$$

where Δ is the first miniband width, and k' is the wavenumber of the electron wave packet corresponding to the electron quasi-momentum $p = \hbar k'$ (k' should not be confused with the wavenumber of the classical wave, which will be used later).

From this, the group velocity of the electron wave packet can be determined:

$$v(k) = \frac{1}{\hbar}\frac{\mathrm{d}\varepsilon}{\mathrm{d}k'} = \frac{\Delta d}{2\hbar}\sin(\mathrm{d}k'). \tag{3}$$

As the electron reaches the BZ boundary, it undergoes Bragg reflection (mathematically expressed as the sign change of the sine function), reversing its k vector and restarting its trajectory from the opposite BZ edge. These oscillations also manifest themselves in real space, typically with nanometric amplitudes [10], and are fundamental to understanding the electron transport properties in SSLs as will be discussed further in Section 4. The real-space displacement of these oscillations can be calculated using the group velocity (Eq. (3)) and the equation of motion for the electron quasi-momentum under the influence of the electrical field,

$$x(t) = \int_0^t \mathrm{d}t' v(k'(t')) = \\ = x(0) - \frac{\Delta}{2eE_0}\cos\left(\frac{eE_0 d}{\hbar}t\right), \tag{4}$$

where $x(0)$ is an initial position of the electron wave packet.

The stationary band transport in nanostructures ($t \gg \tau$) under the action of strong electric fields is shaped by the scattering of electrons with phonons, impurities and by the interface roughness. A notable phenomenon, arising in the miniband transport due to the excitation and further decay of the Bloch oscillations, is the negative dif-

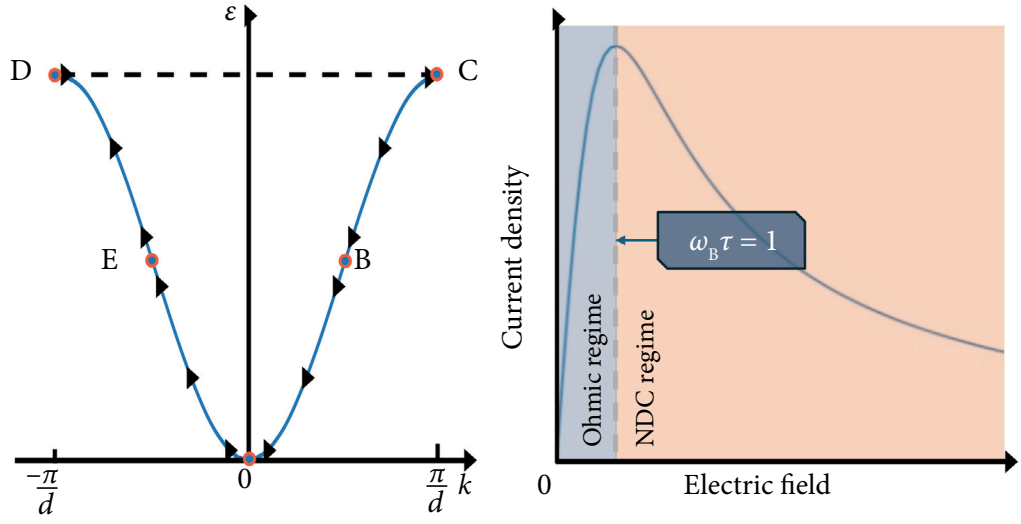

Fig. 3. Left panel: the diagram illustrates Bloch oscillations in the k space along the energy miniband, which is described by the tight-binding approximation in Eq. (2). Initially, the electron wave packet is localized at position A; upon the application of static electric field, the wave packet accelerates, moving through point B towards the Brillouin zone edge at point C. After reaching C, it undergoes Bragg reflection, transitioning to point D (reversing the direction of its motion in real space) and traversing point E as it returns to A. The process then repeats. Right panel: simplified Esaki–Tsu current–field characteristic of a semiconductor superlattice. The blue zone marks the region of Ohmic behaviour while the red shows the negative differential conductivity regime. In terms of the electric field, a grey dashed line indicates the so-called inflexion point ($\omega_B\tau = 1$) or the critical electric field above which the SSL enters the static negative differential conductivity.

ferential conductivity (NDC). It was first theorized by Esaki and Tsu [6], who applied the Boltzmann transport equation to describe the dynamics of the electron ensemble in the momentum space, rather than focusing on individual electron trajectories. Namely, they found the stationary probability distribution function $f(p, t \to +\infty)$ different from the thermal distribution, and then applied it to calculate the drift velocity and current as functions of the applied bias E_0 (see also Ref. [21]). The resulting nonmonotonic current–field characteristic of the SSL has the form

$$j = \frac{\sigma_0 E_0}{1 + (\omega_B \tau)^2}, \tag{5}$$

where $\sigma_0 = n_0 e^2 \tau / m^*$ is the classical Drude's conductivity with n_0, m^* being the electron concentration, the longitudinal (along the axis of the SSL) effective mass of the electron characterized by $m^* = \hbar^2 (\mathrm{d}^2\varepsilon/\mathrm{d}k^2)^{-1} = 2\hbar^2/\Delta d^2$. The current density j is related to the drift velocity of miniband electrons $v_d(E_0)$ as $j = e n_0 v_d$. This nonlinear Esaki–Tsu characteristic, inherent for SSL, is illustrated in Fig. 2 (right panel).

At low electric fields ($\omega_B\tau \ll 1$), the current j is directly proportional to the applied electric field E, following the Ohm's law. However, when the electric field reaches the critical value ($\omega_B\tau = 1$), the slope of the curve becomes negative. In a strong electric field limit ($\omega_B\tau \gg 1$), electrons perform Bloch oscillations between the scattering events and the current decreases inversely with E, i.e. $j \sim 1/E$. In this regime, the current flow in the structure is suppressed, indicating that an electron performs fast oscillations between two points in real space. Differentiating Eq. (5) with respect to E yields the expression for the differential conductivity:

$$\left.\frac{\partial j}{\partial E}\right|_{E=E_0} = \frac{1 - (\omega_B \tau)^2}{(1 + (\omega_B \tau)^2)^2}. \tag{6}$$

The static differential conductivity (6) becomes negative once the condition of Bloch oscillations excitation $(\omega_B\tau) > 1$ is satisfied.

2.1. High-frequency conductivity and gain

As the next step, we consider a response of electrons to the action of the alternating field $E_1 e^{-i\omega t}$, which is characterized by the high-frequency complex conductivity $\sigma(\omega) = \sigma_R + i\sigma_I$ following the relation

$$j(t) = \mathrm{Re}(\sigma(\omega)\, E_1 e^{-i\omega t}). \tag{7}$$

The concept of the high-frequency conductivity is suitable for oscillations and waves of different origin, including electromagnetic, electrostatic, and in some cases acoustical waves [22].

To understand the physical meaning of the real part of conductivity σ_R, one can calculate the mean power per cycle ($T = 2\pi/\omega$) dissipated in the conductor:

$$\begin{aligned}\overline{P} &= \frac{1}{T}\int_0^T j(t')E(t')\mathrm{d}t' = \\ &= \frac{1}{T}\int_0^T E_1[\sigma_R \cos(\omega t') + \sigma_I \sin(\omega t')]E_1 \cos(\omega t')\mathrm{d}t' = \\ &= \sigma_R \frac{E_1^2}{2}.\end{aligned} \tag{8}$$

From Eq. (8) it follows that the power is directly proportional to the real part of the complex conductivity. It is important to emphasize that a positive sign for power indicates absorption, while a negative sign indicates gain. It can be also shown that σ_I determines the dispersive properties of the involved wave. In particular, for the electromagnetic wave (light) the coefficient of absorption (or gain) measured in cm^{-1} is directly proportional to σ_R, and the chromatic dispersion of the refractive index is controlled by σ_I. In the next sections, we will consider how to calculate σ within several models of miniband SSLs.

2.2. Quasistatic conductivity without dispersion

In this simplest model of the high-frequency conductivity, it is assumed that the current $j(t)$ adiabatically follows variations of the alternating field, and therefore technically the total field $E(t) = E_0 + E_1\cos(\omega t)$ can be substituted in the static $j(E)$ characteristic instead of the constant field E_0. Intuitively, it is clear that this approach is valid if the period $T \sim 1/\omega$ is much larger than the time interval during which the static $j(E)$ characteristic is established due to electron scattering, that is the condition $\omega\tau \ll 1$. It is worth noting that the quasistatic approach is the standard tool used in various models of bulk semiconductors [22].

To calculate the small-signal conductivity in SSL, we additionally suppose that $E_1 \ll E_0$ and get

$$j \approx j_{\mathrm{dc}}(E_0) + \left.\frac{\partial j}{\partial E}\right|_{E=E_0} \cdot E_1 \cos(\omega t), \tag{9}$$

where $j_{\mathrm{dc}}(E_0)$ is the static part of the current density and the derivative for the Esaki–Tsu characteristic is calculated in Eq. (6). Following the definition of the average power and using Eq. (7), we have

$$\begin{aligned}\overline{P_\omega} &= \frac{1}{T}\int_0^T j(t')E_1\cos(\omega t')\mathrm{d}t' \approx \\ &\frac{1}{T}\int_0^T \left(j_{\mathrm{dc}}(E_0) + \left.\frac{\partial j}{\partial E}\right|_{E=E_0} \cdot E_1\cos(\omega t') \right) \times \\ &\times E_1\cos(\omega t')\mathrm{d}t' = \\ &= \left.\frac{\partial j}{\partial E}\right|_{E=E_0} \frac{E_1^2}{2}.\end{aligned} \tag{10}$$

Comparing this to Eq. (8), we get that the real part of the quasistatic conductivity is

$$\begin{aligned}\sigma^{\mathrm{quasist}} &= \left.\frac{\partial j}{\partial E}\right|_{E=E_0} = \\ &= \sigma_0 \frac{1-(\omega_B\tau)^2}{(1+(\omega_B\tau)^2)^2}\end{aligned} \tag{11}$$

and its imaginary part is zero. Therefore, there is no dispersion in the quasistatic model.

Furthermore, we will show later that the result (11) coincides with the low-frequency limit of KSS conductivity (15), and this confirms the intuitive criterium of the quasistatic model validity in the form $\omega\tau \ll 1$.

3. Ktitorov model: conductivity with temporal dispersion

In 1971, Ktitorov and co-workers developed a minimal model describing SSL linear response under the influence of the strong constant electric field [16]. This semiclassical model remains valid as long as the electric field is large enough to allow for Bloch oscillations and the NDC regime, but is small enough to have enough Wannier–Stark

levels compared to the miniband width, that is $\hbar\omega_B/\Delta \ll 1$.

By expressing the band in the tight-binding approximation (Eqs. (2, 3)), Ktitorov and co-workers solved the time-dependent Boltzmann transport equation for the distribution function $f(p, t)$ under the assumption of weak perturbation by the alternating field $E_1(\omega)e^{-i\omega t}$, found the time-dependent current, and then following Eq. (7) obtained the expression for the small-signal, high-frequency conductivity

$$\sigma(\omega) = \frac{\sigma_0}{1+\omega_B^2\tau_p\tau_e} \times \\ \times \frac{1-\omega_B^2\tau_p\tau_e - i\omega\tau_e}{(\omega_B^2-\omega^2)\tau_p\tau_e + 1 - i\omega(\tau_p+\tau_e)}, \quad (12)$$

where τ_p and τ_e are momentum and energy relaxation times, respectively.

This result revealed several important findings regarding high-frequency properties of SSLs. First, in the low-frequency limit, $\sigma(\omega)$ reduces to the static differential conductivity (cf. Eq. (6)), which becomes negative when $\omega_B^2\tau_p\tau_e > 1$. This condition marks the onset of NDC and broadband gain for low-frequency waves (11), a key feature in SSL-based high-frequency applications. Second, particularly when the τ_e significantly exceeds τ_p and the Bloch frequency ω_B approaches zero, SSL conductivity (12) resembles the familiar expression for free carrier absorption in the Drude model.

Third, the conductivity (Eq. (12)) demonstrates a strong temporal dispersion, which is directly controlled by Bloch frequency. In particular, for $\omega_B^2\tau_p\tau_e \gg 1$, the real part of $\sigma(\omega)$ not only can turn negative for the frequencies ranging from $\omega = 0$ to almost $\omega = \omega_B$, but also there exists a gain resonance – a range of frequencies where gain is enhanced (Fig. 4). Position of the gain resonance depends on the ratio of the scattering times τ_p/τ_e, and in the case when the scattering times are not very different from each other, the gain resonance is located rather close to Bloch frequency.

Lastly, the model can potentially describe the amplification of longitudinal electrostatic waves, alternatively known as the space-charge waves. In this regard, the KSS model is universal as it can be applied to both electromagnetic and electrostatic waves. However, effects of the spatial dispersion are not included in the KSS model.

4. Ignatov–Shaskin model: conductivity with temporal and spatial dispersion

This model focuses on studying the excitation of space-charge waves in semiconductor superlattices under the influence of the static and uniform electric field E_0 that has the strength large enough to induce Bloch oscillations. The authors adopt

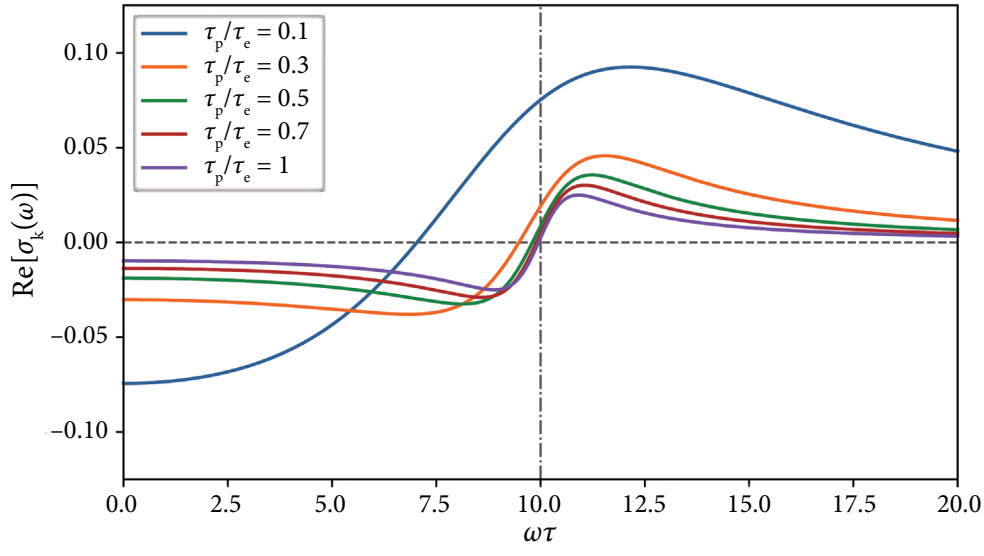

Fig. 4. Comparison of the real part of Ktitorov's et al. conductivity (Eq. (12)) with different ratios of momentum and energy scattering times τ_p/τ_e. The gain resonance can be located close to the Bloch frequency. Dash-dotted line shows $\omega_B\tau_e = 10$.

initial assumptions similar to those in the study by Ktitorov et al., but here they incorporate spatial dispersion in their analysis by considering high-frequency field perturbation in the form of the plane wave with the frequency ω and the wavenumber k. To describe the response of the electrons to external fields, the most full form of Boltzmann transport equation with the Bhatnagar–Gross–Krook (commonly known as BGK) collision integral is used [23]. In contrast, Ktitorov's et al. study utilized a simplified kinetic equation without a spatial variable that accounted only for the main features of the relaxation processes. The BGK integral is defined as [23]

$$St = -\frac{1}{\tau}\left(f - \frac{n(x)}{n_0} f_0 \right), \tag{13}$$

where $f \equiv f(p, x, t)$ is the distribution function satisfying the Boltzmann transport equation, $f_0 \equiv f_0(p)$ is the thermal equilibrium distribution function, $n(x)$ is the electron density distribution across the superlattice, and n_0 is the thermal equilibrium electron density. The density of space charge $n(x)$ is connected to the total field acting on electrons by Poisson's equation, specifying the electrostatic nature of the excited space-charge waves. By linearizing the Boltzmann transport equation under the assumptions that the high-frequency electric field and perturbations of the distribution function are confined within the SSL structure along the axis of the superlattice $0 < x < L$, one can find the high-frequency conductivity

$$\sigma(\omega,k) = \frac{-\varepsilon_0 \varepsilon'}{\tau} \sum_{m,s=-\infty}^{+\infty} \frac{(-\mathrm{i})^m I_m(\Delta/2T)}{I_0(\Delta/2T)} \times \\ \times \left[1 - \frac{\omega_\mathrm{p}^2 m}{\beta\omega_\mathrm{B}\left(\frac{1}{\tau} + \mathrm{i}\, m\omega_\mathrm{B}\right)} \right] \frac{s J_s(\beta) J_{s+m}(\beta)}{\alpha - s}, \tag{14}$$

where $J_s(\beta)$ is Bessel's function, $\beta = k\Delta d/2\hbar\omega_\mathrm{B}$ is the normalized wavenumber that is scaled to the amplitude of the Bloch oscillations in space (cf. Eq. (4)), $\omega_\mathrm{p} = (n_0 e^2/m^* \varepsilon_0)^{1/2}$ is the plasma frequency, $I_m(\Delta/2T)$ is the temperature-dependent transport factor defined by modified Bessel's function, and $\alpha = -(\omega + \mathrm{i}/\tau)/\omega_\mathrm{B}$. It has to be noted that β is a control parameter which accounts for spatial dispersion in high-frequency conductivity (14), so that the dispersion becomes strong, i. e. $\beta \to 1$, when the wavelength approaches the amplitude of the Bloch oscillations in space.

In a long wavelength limit, or, in other words when $\beta \to 0$, the IS conductivity (14) reduces to the KSS conductivity if one considers that $\tau_p = \tau_e = \tau$:

$$\sigma(\omega, k \to 0) = \\ = \frac{\sigma_0}{(1+(\omega_\mathrm{B}\tau)^2)} \frac{1-(\omega_\mathrm{B}\tau)^2 - \mathrm{i}\omega\tau}{(\omega_\mathrm{B}^2 - \omega^2)\tau^2 + 1 - 2\mathrm{i}\omega\tau} \times \\ \times \frac{\sigma_0}{(1+(\omega_\mathrm{B}\tau)^2)} \frac{1-(\omega_\mathrm{B}\tau)^2 - \mathrm{i}\omega\tau}{(\omega_\mathrm{B}\tau)^2 - (\omega\tau + \mathrm{i})^2}. \tag{15}$$

Note that $\omega_\mathrm{B}\tau$ and $\omega\tau$ are dimensionless variables. From here, for simplicity reasons, we will consider that $\sigma_0 = 1$.

At $\omega_\mathrm{B}\tau \to 0$, the high-frequency conductivity (Eq. (15)) is reduced to

$$\sigma(\omega, k \to 0) = \frac{1 - \mathrm{i}\omega\tau}{(\mathrm{i} + \omega\tau)^2}, \tag{16}$$

which is the SL free carrier absorption.

At the limit of low frequencies ($\omega \to 0$), Eq. (15) becomes

$$\sigma(\omega \to 0, k \to 0) = \frac{1-(\omega_\mathrm{B}\tau)^2}{(1+(\omega_\mathrm{B}\tau)^2)^2}. \tag{17}$$

Remarkably, this equation is identical to Eq. 11), which is the quasistatic conductivity of the Esaki–Tsu characteristic.

5. Numerical comparison

We compare Ignatov's Eq. (14) and Ktitorov's Eq. (12) models using numerical calculations implemented in Python. Initially, we demonstrate that at a long wavelength limit – where no spatial dispersion is present (i.e. we set the numerical value of the normalized wave vector to $\beta = 0.001$) – the models correspond closely to one another.

Additionally, we neglect the temperature dependence of the high-frequency conductivity by assuming that the ratio of the modified Bessel functions $I_m(\Delta/2T)/I_0(\Delta/2T) \approx 1$. Considering that the miniband width Δ can range from approximately 4 to 80 meV [24], and that the highest working temperature of a compact quantum cascade laser is around 250 K [25], this is

a reasonable approximation, particularly in lower temperatures.

Our analysis reveals that the summation indices in Eq. (14) m, s are limited to ±1 and 0. As it will be shown later, these indices are sufficient to accurately model the high-frequency (HF) conductivity. For numerical calculations, we select three values of $\omega_B\tau$: 0.25, 1 and 10. The first value illustrates the behaviour of HF conductivity in the Ohmic regime (see Fig. 3), the second examines the behaviour near the inflection point, and the third is high enough to satisfy the gain resonance condition $\omega_B^2\tau_p\tau_e \gg 1$ as introduced by KSS [16].

These values are denoted by grey dashed-dotted lines in Figs. 5–8. For practical purposes, both models are analyzed using dimensionless parameters. This is achieved primarily by multiplying the frequencies by the scattering constant τ. Typical values of the scattering constant in semiconductor superlattices are of an order of 0.1 ps [11]. Thus, for the choice $\omega\tau = 1$ [12], the corresponding frequencies range from 0.1 to 10 THz depending on the scattering constant.

Taking the general form of Ignatov's conductivity (Eq. (14)) and examining the terms in brackets,

$$\frac{1}{\tau} - \frac{\omega_p^2 m}{\beta\omega_B\tau(1/\tau + im\omega_B)}, \tag{18}$$

we multiply the brackets by τ/τ and use $\omega_p^2\tau = \sigma_0/\varepsilon'\varepsilon_0$. Redistributing the terms yields,

$$\frac{\sigma_0}{\varepsilon'\varepsilon_0}\left[\frac{\varepsilon'\varepsilon_0}{\tau\sigma_0} - \frac{m}{\beta\omega_B\tau(1+im\omega_B\tau)}\right], \tag{19}$$

from Ref. [26] we know that the dielectric (Maxwell) relaxation time of the conductor can be expressed as

$$\tau_c = \frac{\varepsilon'\varepsilon_0}{\sigma_0}. \tag{20}$$

Substituting this into the brackets and redistributing terms result in the dimensionless form of Ignatov's equation:

$$\sigma(\omega,k) = -\sigma_0\sum_{m,s}\frac{(-i)^m I_m(\Delta/2T)}{I_0(\Delta/2T)}\times \\ \times\left[\frac{\tau_c}{\tau} - \frac{m}{\omega_B\tau\beta(im\omega_B\tau+1)}\right]\frac{sJ_s(\beta)J_{s+m}(\beta)}{\alpha - s}. \tag{21}$$

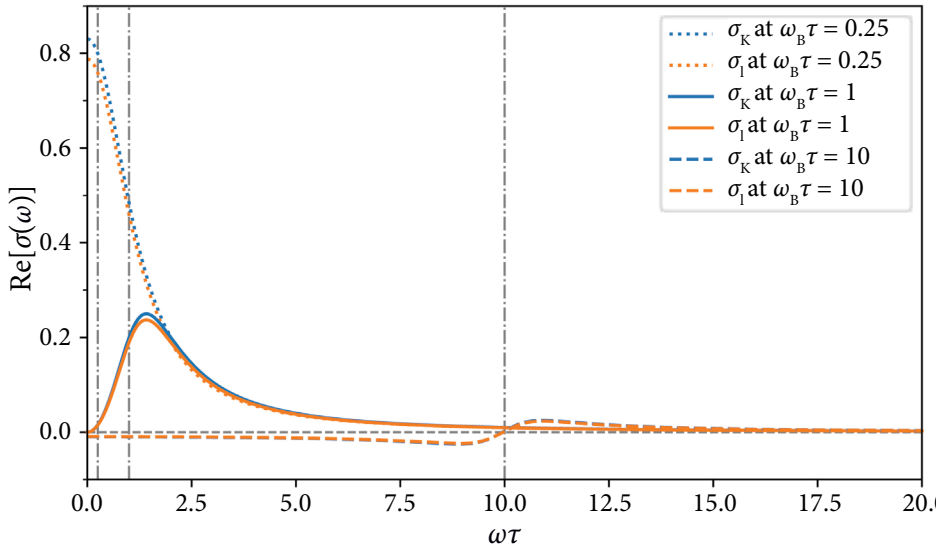

Fig. 5. Comparison of the real parts of Ktitorov's conductivity σ_K (blue dotted line: $\omega_B\tau = 0.25$; blue solid line: $\omega_B\tau = 1$; blue dashed line: $\omega_B\tau = 10$) with Ignatov's HF conductivity at a long wavelength limit $\sigma_I(\omega, k \to 0)$ (orange dotted line: $\omega_B\tau = 0.25$; orange solid line: $\omega_B\tau = 1$; orange dashed line: $\omega_B\tau = 10$). Three grey dash-dotted lines depict the values of $\omega_B\tau$ for separate cases. Here $\beta = 0.001$, $I_m(\Delta/2T)/I_0(\Delta/2T) \approx 1$ and $\tau_c/\tau = 0.1$. Note the positive real part conductivity (absence of gain) at low electric fields $\omega_B\tau = 0.25$, and the negative real part conductivity above the critical electric field, $\omega_B\tau > 1$, indicating the presence of gain.

Note that τ_c/τ is one of the control parameters in our calculations, and the conductivities σ are now scaled to σ_0 in both models under consideration.

The calculated real and imaginary parts of the conductivity for both models – Ktitorov $\sigma_K(\omega)$ and Ignatov $\sigma_I(\omega, k \to 0)$ – are shown in Figs. 5 and 6, respectively. First, it can be seen that the two models correspond well on both the real and imaginary axes at various values of $\omega_B\tau$. Additionally, the absolute values of conductivity, for both the real and imaginary components decrease with increasing electrical field strength.

In Fig. 5, we can discern the resonance predicted by KSS at $\omega \approx \omega_B$ for the case of large $\omega_B\tau = 10$. At low electric field strengths, the resonance shifts to lower frequencies than the predicted resonant frequency because the resonance gain condition is not fully satisfied.

At this resonant frequency, the sign of the conductivity transitions to positive, and the SSL enters the absorption regime. Furthermore, at high electrical fields ($\omega_B\tau > 1$) and in the frequency range $0 < \omega < \omega_B$, the real part of conductivity is negative, confirming the Bloch oscillator's oscillation within this range as described in Ref. [12]. At low field values, the conductivity is positive across the entire frequency range of the ac field, indicating absorption within the SSL. In the ohmic regime ($\omega_B\tau = 0.25$), the maximum absorption occurs at zero frequency with a peak value of 0.85, and this is qualitatively consistent with Eq. (17).

At the critical electrical field ($\omega_B\tau > 1$), the maximum peaks at 0.25 at $\omega\tau = 1.42$. When SSL operates in the NDC regime and the gain criterion is satisfied ($\omega_B\tau > 10$), the maximum gain value (See Eq. (8)) is $\mathrm{Re}[\sigma] = -0.025$ at $\omega\tau \approx 8.89$. This confirms that amplification occurs in SSLs under the influence of large electric fields when $\omega_B^2\tau^2 \gg 1$.

Figure 6, which depicts the imaginary part of the conductivity, shows a peak at the lowest electric field and two distinct dips for the critical electrical field and the NDC regime. The peak value for the lowest field reaches $\mathrm{Im}[\sigma] \approx -0.42$ at $\omega\tau \approx 1$. At the critical electric bias, the dip shifts to lower than resonant frequencies, with the extremum value being $\mathrm{Im}[\sigma] \approx -0.12$ at $\omega\tau \approx 0.74$. At the highest field, the dip aligns with the resonant Bloch frequency reaching a minimum value of $\mathrm{Im}[\sigma] \approx -0.05$ at $\omega\tau \approx 9.95$. Similar to Fig. 5, we attribute this shift to the unfulfilled resonance gain condition. The peak at $\omega\tau = 2.72$, with a maximum value of $\mathrm{Im}[\sigma] \approx 0.125$, vanishes at the highest field, and the line shape begins to follow the Lorentzian profile.

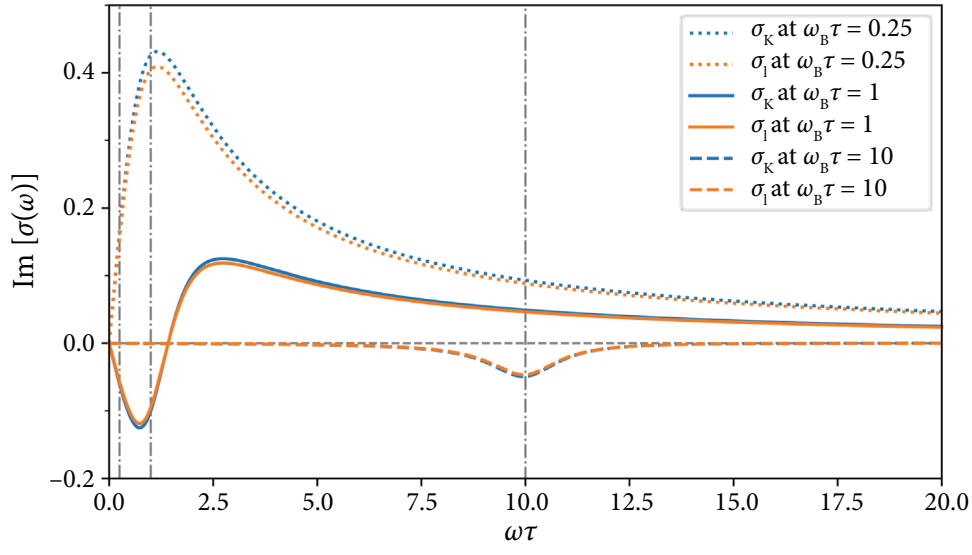

Fig. 6. Comparison of the imaginary parts of the Ktitorov's conductivity σ_K (blue dotted line: $\omega_B\tau = 0.25$; blue solid line: $\omega_B\tau = 1$; blue dashed line: $\omega_B\tau = 10$) with Ignatov's HF conductivity at a long wavelength limit $\sigma_I(\omega, k \to 0)$ (orange dotted line: $\omega_B\tau = 0.25$; orange solid line: $\omega_B\tau = 1$; orange dashed line: $\omega_B\tau = 10$). Three grey vertical dash-dotted lines depict values of $\omega_B\tau$ for separate cases. Here $\beta = 0.001$, $I_m(\Delta/2T)/I_0(\Delta/2T) \approx 1$ and $\tau_c/\tau = 0.1$.

Focusing on the numerical value of the normalized wavenumber β, we estimate that for typical SSL parameters the values of β can approach 0.1 or larger. This range implies that spatial dispersion begins to play a role in the system's description, making the IS model more accurate than the KSS model to describe space-charge waves under these conditions.

This difference is evident in Fig. 7 (real part of conductivity) and Fig. 8 (imaginary part), where the Ktitorov's model ($\sigma_K(\omega)$) is compared to the Ignatov's model ($\sigma_I(\omega, k)$) at $\beta = 0.1$. The main parameters are consistent with the previously analysed case of $\beta \to 0$. As shown, the models remain similar in the Ohmic regime and near the critical electric field ($\omega_B\tau = 0.25$ and $\omega_B\tau = 1$) and undergo a minimal change. However, significant deviations appear at the highest field ($\omega_B\tau = 10$).

In Fig. 7, examining the real part of the conductivity, we see that the peak gain for the large field case has doubled from $\mathrm{Re}[\sigma] \approx -0.025$ to -0.05 and shifted to a higher frequency near the resonant Bloch frequency. Additionally, the introduction of spatial dispersion extends the gain region up to $\omega\tau \approx 11.05$, and the absorption peak observed in Ktitorov's results disappears (see Fig. 7).

Analysing the imaginary part of the conductivity in Fig. 8, we find that at the large electric field, the line shape deviates from the Lorentzian profile. A new positive peak emerges, and the drop shifts to higher frequencies. The maximum value of the imaginary part of Ignatov's conductivity reaches 0.008 at $\omega\tau \approx 12.37$, while the minimum value remains largely unchanged but shifts to a higher frequency at $\omega\tau \approx 10.41$.

To summarize, we briefly overviewed and considered basic semiclassical models describing the high-frequency conductivity of electrically biased semiconductor quantum superlattices. The main attention was attributed to the well-known Ktitorov et al. model and the less admitted, but more advanced model of Ignatov and Shashkin that considers effects of spatial dispersion at the long-wavelength limit, and the models show good agreement across varying electric biases. This agreement persists with the inclusion of spatial dispersion at relatively low field values, where either the bias is below the critical one required for the onset of NDC or a strong gain resonance is not yet reached.

However, at high electric fields, the spatial dispersion becomes crucial, significantly altering

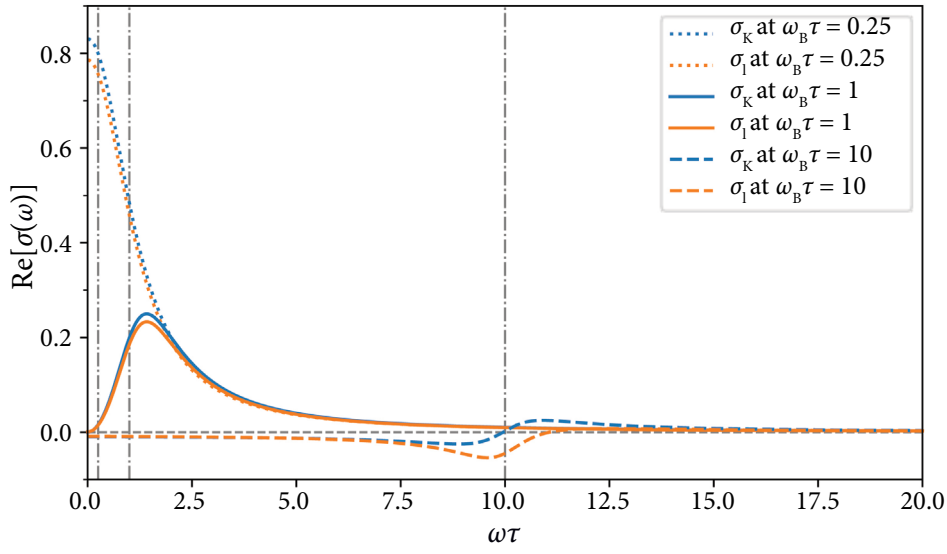

Fig. 7. Comparison of the real parts of Ktitorov's conductivity σ_K (blue dotted line: $\omega_B\tau = 0.25$; blue solid line: $\omega_B\tau = 1$; blue dashed line: $\omega_B\tau = 10$) with Ignatov's HF conductivity $\sigma_I(\omega, k)$ at $\beta = 0.1$ (orange dotted line $\omega_B\tau = 0.25$; orange solid line $\omega_B\tau = 1$; orange dashed line $\omega_B\tau = 10$). Two grey vertical dash-dotted lines depict values of $\omega_B\tau$ for separate cases. Here, $I_m(\Delta/2T)/I_0(\Delta/2T) \approx 1$ and $\tau_c/\tau = 0.1$.

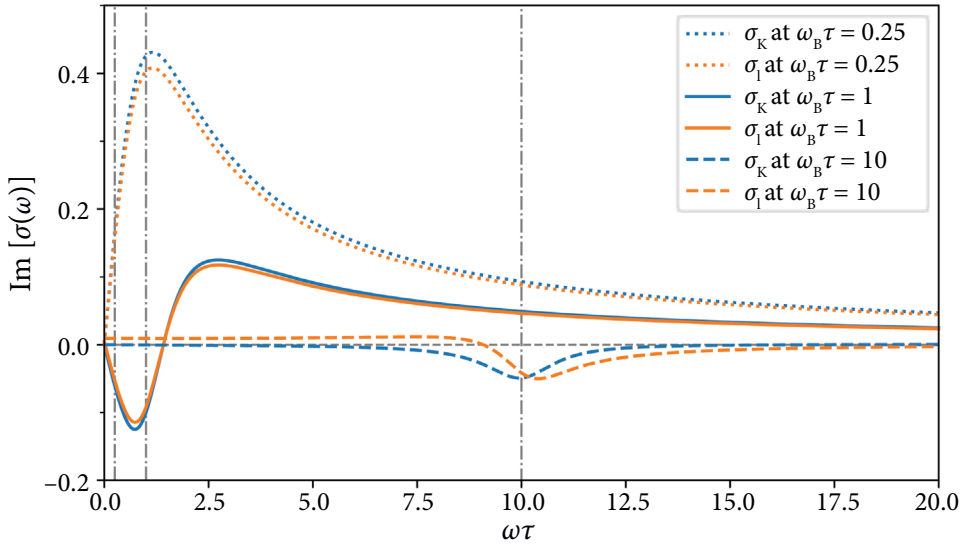

Fig. 8. Comparison of the imaginary parts of Ktitorov's conductivity $\sigma_K(\omega)$ (blue dotted line: $\omega_B\tau = 0.25$; blue solid line: $\omega_B\tau = 1$; blue dashed line: $\omega_B\tau = 10$) with Ignatov's HF conductivity $\sigma_I(\omega, k)$ at $\beta = 0.1$ (orange dotted line $\omega_B\tau = 0.25$; orange solid line $\omega_B\tau = 1$; orange dashed line $\omega_B\tau = 10$). Two grey vertical dash-dotted lines depict values of $\omega_B\tau$ for separate cases.

the results. This highlights the need for further research into effects of the spatial dispersion under fully met gain criteria. Leveraging the insights and comparative analysis acquired from the presented models, deliberate strategies for the design of devices dedicated to high-frequency gain relying on the negative differential conductivity can be developed.

6. The physics beyond the used approximations

To begin, it is worth mentioning a very interesting work by Willenberg et al. dedicated to the generalization of the KKS theory using density matrix formalism [27]. The model considered a sequential tunnelling regime in quantum structures with thick barriers and allowed one to unveil a surprising link between the Bloch gain mechanism in periodic semiconductor superlattices and quantum cascade laser structures. Next, as the original theory was limited to the analysis of the small signal case, an important step in its extension was the consideration of a large signal case [28, 29]. It was revealed that for parameters satisfying the small-signal gain conditions, the gain as a rule also exists for quite large amplitudes of the amplified field. Moreover, it was exposed that in the large-signal regime, the dependence of the time-averaged current on the applied bias has a positive slope, which is a high-frequency counterpart of the limited space-charge accumulation effect known in the bulk semiconductors with NDC [22]. An elegant model based on the superlattice balance equation requires a special underline: it allows one to establish a profound link between the carrier dynamics in superlattice and the dynamics of Josephson junctions [30], indicating that electromagnetic radiation can occur due to multiphoton emission and can reach THz frequencies.

6.1. Related experiments and outlook

Currently, there exist only a few basic experiments devoted to the Bloch gain. Firstly, Savvidis and co-workers revealed that the frequency-dependent crossover from loss to gain related to the Stark ladder, produced by the applied dc electric field, can be observed in InAs/AlSb superlattice structures [12]. A combination of sub-critical doping and a novel technological approach relying on the insertion of heavily doped InAs regions allowed one to suppress propagating high-field domains. The employment of free electron lasers to deliver the frequency-tuneable THz radiation which is coupled to waveguides loaded with the InAs/AlSb superlattice mesas allowed the displaying of clear signatures

of the Bloch gain at 1.98 THz. Furthermore, in the framework of the KSS model, it was demonstrated that the crossover from loss to gain depends on the frequency; the higher the frequency, the higher the voltage or the Stark splitting required to sense the suppression of the real dynamical conductance are [12]. Secondly, Sekine and Hirakawa observed dispersive peculiarities in the spectral shape of the complex conductivity of Bloch oscillating electrons in GaAs/AlGaAs SSLs by using the time-domain THz electro-optic sampling technique [31]. The theoretical justification of the experiment was done for simplicity by assuming a small amplitude of the ac probe field corresponding to a linear response, which is not always satisfied in conditions of real experiments [31]. Thirdly, the Bloch gain was revealed in a specially designed quantum cascade structure suitable for lasing in the infrared range [32]. Terazzi et al. studied this quantum cascade laser operation in the condition of a weak to vanishing population inversion. The observed effect was interpreted in terms of the dispersive shape of the gain spectrum, its dependence on the active region design, and additionally supported by theoretical calculations [27, 32]. It is worth emphasizing that in all the aforesaid works the amplified wave was assumed to be of electromagnetic origin, although in both theoretical contributions [16, 17] it was speculated that the wave can also be treated as an electrostatic space charge wave propagating with the drift velocity of miniband electrons.

Recently, our group observed the dissipative parametric high-frequency gain in SSLs at room temperature [33] and explained it in the line with an extension of the semiclassical model [34]. One of the most exciting findings of the work [33] uncovers the significant role played by the propagating slow electrostatic waves in the high-frequency gain mechanism. Excitation of slow electrostatic waves in the sub-critically doped superlattice not only provides a significant enhancement of the gain coefficient [33], but also can determine the coexistence of Bloch and parametric mechanisms of high-frequency gain [35, 36]. These observations open a pathway to systematical investigation of the effects of space charge waves under the Bloch gain conditions in quantum semiconductor superlattices.

References

[1] G. Valušis, A. Lisauskas, H. Yuan, W. Knap, and H.G. Roskos, Roadmap of terahertz imaging 2021, Sensors **21**, 4092 (2021).

[2] Y. Huang, Y. Shen, and J. Wang, From terahertz imaging to terahertz wireless communications, Engineering **22**, 106 (2023).

[3] Z. Zhou, A. Kassem, J. Seddon, E. Sillekens, I. Darwazeh, P. Bayvel, and Z. Liu, 938 Gb/s, 5–150 GHz ultra-wideband transmission over the air using combined electronic and photonic-assisted signal generation, J. Lightwave Technol. **42**, 7247 (2024).

[4] M. Asada and S. Suzuki, Terahertz emitter using resonant-tunneling diode and applications, Sensors **21**, 1384 (2021).

[5] M.S. Vitiello and P. De Natale, Terahertz quantum cascade lasers as enabling quantum technology, Adv. Quantum Tech. **5**, 2100082 (2022).

[6] L. Esaki and R. Tsu, Superlattice and negative differential conductivity in semiconductors, IBM J. Res. Dev. **14**, 61 (1970).

[7] E.L. Ivchenko and G.E. Pikus, *Superlattices and Other Heterostructures: Symmetry and Optical Phenomena*, Vol. 110 (Springer Berlin Heidelberg, Berlin, Heidelberg, 1997).

[8] J. Feldmann, K. Leo, J. Shah, D.A.B. Miller, J.E. Cunningham, T. Meier, G. Von Plessen, A. Schulze, P. Thomas, and S. Schmitt-Rink, Optical investigation of Bloch oscillations in a semiconductor superlattice, Phys. Rev. B **46**, 7252 (1992).

[9] C. Waschke, H.G. Roskos, R. Schwedler, K. Leo, H. Kurz, and K. Köhler, Coherent submillimeter-wave emission from Bloch oscillations in a semiconductor superlattice, Phys. Rev. Lett. **70**, 3319 (1993).

[10] V.G. Lyssenko, G. Valušis, F. Löser, T. Hasche, K. Leo, M.M. Dignam, and K. Köhler, Direct measurement of the spatial displacement of Bloch-oscillating electrons in semiconductor superlattices, Phys. Rev. Lett. **79**, 301 (1997).

[11] K.F. Renk, B.I. Stahl, A. Rogl, T. Janzen, D.G. Pavel'ev, Yu.I. Koshurinov, V. Ustinov, and A. Zhukov, Subterahertz superlattice parametric oscillator, Phys. Rev. Lett. **95**, 126801 (2005).

[12] P.G. Savvidis, B. Kolasa, G. Lee, and S.J. Allen, Resonant crossover of terahertz loss to the gain of a Bloch oscillating InAs/AlSb superlattice, Phys. Rev. Lett. **92**, 196802 (2004).

[13] A. Lisauskas, C. Blöser, R. Sachs, H.G. Roskos, A. Juozapavičius, G. Valušis, and K. Köhler, Time-resolved photocurrent spectroscopy of the evolution of the electric field in optically excited superlattices and the prospects for Bloch gain, Appl. Phys. Lett. **86**, 102103 (2005).

[14] T. Hyart, N.V. Alexeeva, J. Mattas, and K.N. Alekseev, Terahertz Bloch oscillator with a modulated bias, Phys. Rev. Lett. **102**, 140405 (2009).

[15] A. Wacker, Coexistence of gain and absorption, Nature Phys. **3**, 298 (2007).

[16] S.A. Ktitorov, G.S. Simin, and V.Y. Sindalovskii, Bragg reflections and high-frequency conductivity of an electronic solid-state plasma, Sov. Phys. Solid State **13**, 1872 (1972).

[17] A.A. Ignatov and V.I. Shashkin, Bloch oscillations of electrons and instability of space-charge waves in superconductor superlattices, Sov. Phys. JETP **66**, 526 (1987).

[18] F.G. Bass and A.P. Tetervov, High-frequency phenomena in semiconductor superlattices, Phys. Rep. **140**, 237 (1986).

[19] E.E. Mendez, F. Agulló-Rueda, and J.M. Hong, Stark localization in GaAs-GaAlAs superlattices under an electric field, Phys. Rev. Lett. **60**, 2426 (1988).

[20] M. Dignam, J.E. Sipe, and J. Shah, Coherent excitations in the Stark ladder: excitonic Bloch oscillations, Phys. Rev. B **49**, 10502 (1994).

[21] V. Karpus, *Dvimačiai elektronai* (Ciklonas, 2004), [in Lithuanian].

[22] J. Požela, *Plasma and Current Instabilities in Semiconductors: International Series on the Science of the Solid State* (Elsevier Science, Burlington, 1981).

[23] P.L. Bhatnagar, E.P. Gross, and M. Krook, A model for collision processes in gases. I. Small amplitude processes in charged and neutral one-component systems, Phys. Rev. **94**, 511 (1954).

[24] X.L. Lei, N.J.M. Horing, H.L. Cui, and K.K. Thornber, One-dimensional confinement effects on miniband transport in a semiconductor superlattice, Phys. Rev. B **48**, 5366 (1993).

[25] A. Khalatpour, A.K. Paulsen, C. Deimert, Z.R. Wasilewski, and Q. Hu, High-power portable terahertz laser systems, Nat. Photonics **15**, 16 (2021).

[26] A.E. Seaver, An equation for charge decay valid in both conductors and insulators, arXiv:0801.4182

[27] H. Willenberg, G.H. Döhler, and J. Faist, Intersubband gain in a Bloch oscillator and quantum cascade laser, Phys. Rev. B **67**, 085315 (2003).

[28] H. Kroemer, Large-amplitude oscillation dynamics and domain suppression in a superlattice Bloch oscillator, arXiv:cond-mat/0009311

[29] T. Hyart, K.N. Alekseev, and E.V. Thuneberg, Bloch gain in dc-ac-driven semiconductor superlattices in the absence of electric domains, Phys. Rev. B **77**, 165330 (2008).

[30] A.A. Ignatov, K.F. Renk, and E.P. Dodin, Esaki-Tsu superlattice oscillator: Josephson-like dynamics of carriers, Phys. Rev. Lett. **70**, 1996 (1993).

[31] N. Sekine and K. Hirakawa, Dispersive terahertz gain of a nonclassical oscillator: Bloch oscillation in semiconductor superlattices, Phys. Rev. Lett. **94**, 057408 (2005).

[32] R. Terazzi, T. Gresch, M. Giovannini, N. Hoyler, N. Sekine, and J. Faist, Bloch gain in quantum cascade lasers, Nat. Phys. **3**, 329 (2007).

[33] V. Čižas, L. Subačius, N.V. Alexeeva, D. Seliuta, T. Hyart, K. Köhler, K.N. Alekseev, and G. Valušis, Observation of the dissipative parametric gain in a GaAs/AlGaAs superlattice, Phys. Rev. Lett. **128**, 236802 (2022).

[34] T. Hyart, A.V. Shorokhov, and K.N. Alekseev, Theory of parametric amplification in superlattices, Phys. Rev. Lett. **98**, 220404 (2007).

[35] V. Čižas, N. Alexeeva, K.N. Alekseev, and G. Valušis, Coexistence of Bloch and parametric mechanisms of high-frequency gain in doped superlattices, Nanomaterials **13**, 1993 (2023).

[36] V. Čižas, N. Alexeeva, K. Alekseev, and G. Valušis, Sum-frequency generation and amplification processes in semiconductor superlattices, Lith. J. Phys. **63**, 148 (2023).

AUKŠTADAŽNIU LAIDUMU PAGRĮSTŲ TERAHERCINIO STIPRINIMO MODELIŲ KVANTINĖSE PUSLAIDININKINĖSE SUPERGARDELĖSE PALYGINAMASIS TYRIMAS

L. Stakėla, K.N. Alekseev, G. Valušis

Fizinių ir technologijos mokslų centro Optoelektronikos skyrius, Vilnius, Lietuva

Santrauka

Didelės galios, stabilių ir mažų matmenų terahercų (THz) šaltinių, galinčių veikti kambario temperatūroje, kūrimas tebėra vienas didžiausių THz ir kietojo kūno fizikos iššūkių. Nors šiuolaikinių puslaidininkinių prietaisų, tokių kaip rezonansiniai tuneliniai diodai ir kvantiniai kaskadiniai lazeriai, technologija padarė milžinišką pažangą, vis dar susiduriama su tam tikrais iššūkiais, susijusiais su maža spinduliuotės galia, jautrumu temperatūrai ir ribotu dažnio derinimu. Šiuo požiūriu puslaidininkinės supergardelės yra perspektyvios puslaidininkinės kvantinės struktūros kompaktiškiems THz osciliatoriams ir stiprintuvams kurti. Šiame tyrime trumpai apžvelgiami pagrindiniai kvaziklasikiniai modeliai, aprašantys supergardelės aukštadažnį laidumą bei jo dispersines savybes.

Pagrindinis dėmesys skirtas populiariam ir plačiai naudojamam Ktitorovo ir kt. aukštadažnio laidumo dispersiniam modeliui bei mažiau žinomam, bet sudėtingesniam Ignatovo ir Šaškino modeliui, kuris papildomai įskaito ir erdvinę dispersiją bei plazminių bangų susiformavimą. Remdamiesi klasikiniu kvazistatiniu stiprinimo modeliu supergardelėse su neigiamu diferencialiniu laidumu, mes atlikome jų lyginamąją analizę. Šio darbo tikslas – pateikti paprastą įvadą į šiuos modelius ir jų praktinę reikšmę THz prietaisų kūrimui.

The article is dedicated to the memory of Professor Gintautas Jurgis Babonas

It is not enough to voice that Jurgis was visionary and transformative physicist with wide erudition – it is no less important to note the fact that behind all this nestled a multifaceted personality with a formidable intellect and a deep sense of justice. Jurgis' office on the third floor of the former Semiconductor Physics Institute at Goštauto Street was a particular place. The lovely place where you are always welcome to share your new scientific findings and impressions from scientific conferences; the privileged place where you can be heard and be understood; the unique place where you can be encouraged to pursue your dreams... Jurgis' personal spirit, his enthusiasm and positive energy infected those around him.

His impressive visions in physics covered a large variety of topics – new materials and high-temperature superconductivity, semiconductor optics and quasicrystals, innovative measurement techniques and ellipsometry, semiconductor optics and nanostructures… Quantum superlattices and terahertz physics was not an exception – time after time this topic was discussed and considered. As always, all this was surrounded by a subtle smell of coffee… I recall those illuminating conversations, in musical terms, as polyphonic – several topics were developed simultaneously, and sometimes they extrapolated from physics to the totally different fields of classical music and arts…

Although a lot of time has passed since those days, the spirit of these remarkable conversations is not subject to Time. It still inspires us to continue our intriguing scientific journey. It still encourages us to be amazed. It still encourages us not to despair.

I am grateful for Jurgis' generous spirit, which made each of us a better scientist and colleague, better person and teacher…

Gintaras Valušis

1st – 2d December 2024, Antakalnis in Vilnius